International Journal of Greenhouse Gas Control 149 (2026) 104564

Contents lists available at ScienceDirect

International Journal of Greenhouse Gas Control

journal homepage: www.elsevier.com/locate/ijggc

# Influence of $CO_2$ partial pressure on electrochemical behavior of corrosion-resistant alloys for $CO_2$ injection tubing of carbon capture and storage system

Maryam Eslami [#], Xi Wang [##], Yoon-Seok Choi [*]

*Department of Chemical and Biomolecular Engineering, Institute for Corrosion and Multiphase Technology, Ohio University, Athens, OH 45701, United States*

ARTICLE INFO

*Keywords:*
Stainless steel
Passivation
Pitting
Supercritical $CO_2$
Electrochemical characterization

ABSTRACT

Four different corrosion-resistant alloys (13Cr, super 13Cr, 25Cr duplex stainless, 25Cr super duplex stainless steel) were studied under two different $CO_2$ partial pressures (0 and 13.8 MPa) at high temperature (150 °C) in a 3 wt.% NaCl solution. Electrochemical and exposure experiments were conducted at a consistent initial pH for comparison. The results indicate that 13Cr exhibits active corrosion behavior, whereas super 13Cr demonstrates typical passive behavior without re-passivation under the testing conditions. Both 25Cr duplex and 25Cr super duplex steels show exceptional corrosion resistance and passive behavior, with re-passivation potentials higher than corrosion potential in nearly all testing conditions. Passive films show similar composition and forward-scan responses under both experimental conditions; however, in the $CO_2$ environment, the alloys repassivated only at more negative potentials than in the $CO_2$-free condition.

## 1. Introduction

Worldwide concerns regarding climate change have led to extensive efforts and investments to capture and store carbon dioxide ($CO_2$) in secure geologic reservoirs, such as depleted oil and gas wells, to prevent its release into the atmosphere. This process, known as carbon capture and storage (CCS), can significantly mitigate the detrimental impact of fossil fuel use on the climate (Herzog, 2009).

A typical CCS system consists of several components, including a $CO_2$ capture and separation unit, a $CO_2$ compression unit, a $CO_2$ transport unit, a $CO_2$ injection unit, and finally a monitoring unit (Herzog, 2009). The transport and injection units are at risk of degradation due to corrosion. In the transport unit, the captured $CO_2$ is compressed to pressures above its critical point (7.4 MPa, 31 °C) to optimize transportation efficiency through steel pipelines. The supercritical $CO_2$ ($scCO_2$) phase does not cause corrosion to the pipeline if it is completely dehydrated and free of impurities. However, depending on the sources of $CO_2$ and $CO_2$ capture and separation technology, the $scCO_2$ phase often contains impurities such as $H_2O$, $O_2$, $H_2S$, $SO_2$, and $NO_2$. These impurities not only alter the critical point, thereby affecting the density of the $CO_2$ phase, but also increase the corrosion rate (Leung et al., 2014; Li et al., 2023; Sun et al., 2023).

For the injection tubing, the risk of corrosion is low during injection and re-injection. However, during short- and long-term shut-ins, the flowback of formation water, which is present in the injection wells or aquifers, can result in corrosion. In this case, the corrosion is basically due to the dissolution of $CO_2$ in water and the subsequent formation of carbonic acid ($H_2CO_3$) that causes the so-called "sweet corrosion". The mode of corrosion, whether uniform or localized, depends on the material and environmental conditions (Eslami et al., 2024a). In addition to the high partial pressure of $CO_2$, as a necessity for the CCS process, the expected environmental conditions of the injection wells include high temperature (>100 °C) and high salinity ($Cl^-$ concentration as high as 60,000 ppm), resulting in an aggressively corrosive environment (Zhao et al., 2019). As mentioned earlier, the presence of impurities such as $SO_x$ and $NO_x$, in the captured $CO_2$ could further accelerate the corrosion of the injection tubing materials (Choi et al., 2010; Cui et al., 2019; Kairy et al., 2023; Li et al., 2019; Matsuo et al., 2022; Sun et al., 2023). One feasible protection strategy is the application of corrosion-resistant alloys, such as different types of stainless steel, which can withstand corrosion in dense wet $CO_2$ and $CO_2$-saturated formation water and hence can be used in certain sections of transportation and injection

* Corresponding author.
*E-mail address:* choiy@ohio.edu (Y.-S. Choi).
[#] Present address: Illinois Applied Research Institute, College of Engineering, University of Illinois at Urbana-Champaign, Champaign, IL 68210, United States.
[##] Present address: Axalta Coating Systems, 1050 Constitution Ave., Philadelphia, PA 19112, United States.

https://doi.org/10.1016/j.ijggc.2025.104564
Received 11 June 2025; Received in revised form 7 November 2025; Accepted 22 December 2025
Available online 27 December 2025

units when economically feasible (Svenningsen et al., 2023). In this regard, due to economic benefits, low alloy steels (with Cr content up to 6.5 %) (Wei and Gao, 2019) have been studied for CCS applications. The corrosion behavior of these alloys has been compared to that of commonly used carbon steel grades, such as X65 (Hua et al., 2015, 2020) and in some cases to the behavior of stainless steel grades with higher Cr content, such as 316 L (Wei et al., 2016).

Various types of stainless steel, such as 13Cr (Hua et al., 2017; Li et al., 2018; Turnbull and Griffiths, 2003; Zhu et al., 2019), super 13Cr (S13Cr) (Matsuo et al., 2022; Yue et al., 2021, 2020), duplex and super duplex stainless steel (DSS and SDSS, respectively) (Matsuo et al., 2022; Svenningsen et al., 2023) have been investigated to be used for oil and gas production tubing and for $CO_2$ injection tubing in the CCS systems. While the 13Cr class of stainless-steel alloy is a more economical choice, as the research shows, it can expose the system to the risk of failure due to pitting corrosion, especially under more severe conditions. DSS with superior mechanical strength and corrosion resistance is a more reliable option for use in CCS systems. DSS is a class of steel that ideally contains an equal volume fraction of two separate phases, namely ferrite (α) and austenite (γ). As both phases contain more than 10.5 wt. % to 12 wt. % Cr, they are stainless (Haugan et al., 2016; Nilsson, 1992). DSSs usually have 22 wt. % Cr. DSSs with pitting resistance equivalent number (PREN) above 40 are categorized as super duplex stainless steels (SDSS) (Sathirachinda et al., 2011). SDSS is therefore highly resistant to localized corrosion under aggressive conditions and competitive at cost compared to austenitic stainless steel due to its relatively small Ni content (Haugan et al., 2016).

Research has shown a direct correlation between the corrosion rate of 13Cr alloy in oilfield formation water and the partial pressure of $CO_2$ at high temperature (140 °C) (Zhu et al., 2019). The electrochemical behavior of 13Cr changes from a typical passive behavior at lower $pCO_2$ (12 MPa) to a more active corroding behavior at higher $pCO_2$ (28 MPa). The active corrosion behavior at higher $pCO_2$ has been attributed to the instability of the passive film due to the low pH (as low as 2.75) at this condition (Zhu et al., 2019). More recent studies (Zhang et al., 2024) on corrosion of 13Cr in oilfield formation water at high temperature of 200 °C with the addition of $H_2S$ impurity confirm the increase in uniform corrosion rate with $pCO_2$ from 10 MPa to 45 MPa. The same study showed that for S13Cr and 25Cr (DSS), the uniform corrosion rate first decreased and subsequently increased with $pCO_2$, with the critical $pCO_2$ (where the corrosion rate increases) being 25 MPa under these conditions. The pitting corrosion rate decreased with $pCO_2$ for both 13Cr and S13Cr; however, for 25Cr, it showed a maximum at 25 MPa $pCO_2$. More interestingly, the 25Cr alloy showed the highest pitting corrosion rate under the conditions tested, which is unexpected considering the high amount of Cr in this alloy's composition. Other studies on DSS, such as the one by Liu et al. (2021), showed a decrease in pitting resistance with temperature (from 100 °C to 300 °C) and a negligible change in corrosion rate with the increase in $pCO_2$ from 8.4 to 32.8 bar (0.84 MPa to 3.2 MPa). In addition to the presence of $H_2S$ impurity that interferes with the effect of $pCO_2$, especially on the pitting corrosion rate (Soares Costa and Altenhofen, 2024), one common drawback in studies such as the ones cited here (Liu et al., 2021; Zhang et al., 2024; Zhu et al., 2019) is the lack of explicit solution pH control at different $pCO_2$ conditions, resulting in the ambiguity of the role of $CO_2$ in the corrosion mechanism.

Introducing other stimulating factors, such as different impurities ($O_2$, $SO_2$) and flow (shear stress) in a high-pressure $CO_2$ environment, alters and complicates the corrosion behavior of CRAs too. A study by Li et al. (2018) has shown that, under the $scCO_2$ condition (8 MPa $pCO_2$ at 60 °C) introducing the flow velocity of 2 m/s increased the passive current density of 13Cr, however, it did not affect the pitting potential. The addition of a small amount of oxygen (0.1 MPa) to the system, under these dynamic conditions, decreased the passive current density by one order of magnitude. Although the addition of a higher amount of oxygen (1 MPa) reversed this positive effect and resulted in a passive current density similar to that under the condition without oxygen. The authors concluded that both flow and excessive amounts of oxygen result in the instability of the passive film and a higher corrosion rate. However, the presence of ~1 % oxygen in the system can facilitate the formation of a protective passive film. Other researchers, such as Matsuo et al. (2022) have reported a significant increase in the corrosion rate of S13Cr under the $scCO_2$ conditions (130 bar (13 MPa) total pressure at 100 °C) from 0.02 mm/y to 21.94 mm/y by the addition of 0.5 % $SO_2$. This significant increase in the corrosion rate was attributed to the decrease in pH (to 1.9 with 0.5 % $SO_2$) to values lower than the de-passivation pH of S13Cr. In the same study, DSS and SDSS presented excellent resistance to the pitting corrosion under the same conditions, with corrosion rates lower than 0.03 mm/y (<0.01 mm/y for SDSS). This excellent corrosion behavior was due to the negligible influence of $SO_2$ on the composition of the passive film formed on SDSS under the studied experimental conditions.

While all these studies provide valuable insight regarding the materials selection for the $CO_2$ injection unit, the complication in corrosion behavior occurring due to the presence of additional stimulating factors makes it impossible to understand the sole effect of $pCO_2$ on the corrosion behavior. This emphasizes the necessity of performing electrochemical corrosion testing on various CRAs in a pure $scCO_2$ environment to gain a fundamental understanding of the effects of $CO_2$ on their passivation and pitting corrosion. Since, according to the literature, low pH induced by the high $CO_2$ content under $scCO_2$ conditions is the main reason for the deterioration of corrosion properties in this environment (Eslami et al., 2024b), therefore, in this paper, we conducted electrochemical experiments in $scCO_2$ and $N_2$ environments at the same temperature and pH to investigate the effect of $CO_2$ pressure on the corrosion behavior of various CRAs. Electrochemical measurements, including linear polarization resistance (LPR), cyclic potentiodynamic polarization (CPP), and cathodic polarization measurements, were performed on specimens of 13Cr, S13Cr, DSS, and SDSS in both above-mentioned environments. Pitting or active corrosion on the surface after the electrochemical measurements was evaluated by scanning electron microscopy (SEM) and energy dispersive X-ray spectroscopy (EDS). The composition of the passive layers was examined using X-ray photoelectron spectroscopy (XPS).

## 2. Materials and methods

### 2.1. Materials

13Cr, super 13Cr, duplex, and super duplex stainless steels, with the nominal composition provided in Table 1, were used in this study. The exact heat-treatment history of the alloys was not available. However, the objective of this study is to evaluate the corrosion behavior and surface film development under different $CO_2$ environments, rather than to isolate the influence of microstructure.

The specimens for the electrochemical experiments were machined into a cylindrical geometry with a ~5 $cm^2$ exposed area. Additional rectangular-type specimens with ~1 $cm^2$ exposed area were machined for further analysis with XPS. Prior to each experiment, the specimens were grounded up to #600 grit using silicon carbide papers with water flow. They were then rinsed with deionized (DI) water, sonicated in

**Table 1**
Nominal composition of the different grades of stainless steel used in this study.

| | C | Si | Mn | Cr | Mo | Ni |
|---|---|---|---|---|---|---|
| 13Cr | 0.15 ~ 0.22 | ≤ 1.00 | 0.25 ~ 1.00 | 12.0 ~ 14.0 | 0.01 | ≤ 0.5 |
| S13Cr | ≤ 0.03 | ≤ 0.50 | ≤ 0.50 | 11.5 ~ 13.5 | 1.50 ~ 3.00 | 5.0 ~ 6.5 |
| DSS | ≤ 0.03 | ≤ 0.80 | ≤ 7.50 | 24.5 ~ 26.5 | 0.75 ~ 2.00 | 3.5 ~ 6.5 |
| SDSS | ≤ 0.03 | ≤ 0.80 | ≤ 1.20 | 24.0 ~ 26.0 | 3.00 ~ 5.00 | 6.0 ~ 8.0 |

isopropyl alcohol for 60 s, and dried with lab air.

### 2.2. Electrochemical measurements

The high-pressure/high-temperature (HP/HT) corrosion experiments were carried out in a 4 L stainless steel autoclave. A detailed schematic representation of this autoclave is shown in Fig. 1. A typical three-electrode setup, including an HP/HT Ag/AgCl (0.1 M KCl) reference electrode, a cylindrical specimen as the working electrode, and a platinum-coated niobium cylinder as the counter electrode, was used for electrochemical measurements. The reference electrode was calibrated with a saturated Ag/AgCl electrode to ensure the potential difference of ~ 91 mV. A HP/HT $ZrO_2$ pH probe was used to monitor pH during the experiment. This electrode was calibrated at 80 °C and 150 °C prior to each test by the procedure supplied by the manufacturer.[1]

It should be noted that the schematic in Fig. 1 also depicts the holder and the XPS specimens, which were installed in the autoclave and exposed to similar conditions to those of the electrochemical measurements in separate experiments. The details of these experiments will be discussed later in the manuscript.

Two series of experiments were conducted on each material in a 3 wt. % NaCl solution in equilibrium with either $scCO_2$ or $N_2$ environment. The experiments in the $N_2$ environment were designed to investigate the effect of high $CO_2$ partial pressure on electrochemical behavior while maintaining the same solution pH. The test matrix describing the testing conditions for the electrochemical measurements is provided in Table 2.

Experimental procedures were as follows: 3 L of 3 wt. % NaCl solution was prepared and placed in the autoclave. The solution was then sparged with $CO_2$ or $N_2$ gas for at least 3 h for deoxygenation. In the meantime, the temperature of the solution was increased to 80 °C. At this temperature, for the experiments with $N_2$, the pH was adjusted to 2.8 using 1 M HCl solution, which would result in pH 2.9 at 150 °C (based on the pH calculation). After inserting the working, reference, and pH electrodes, the autoclave was sealed while purging with $CO_2$ (or $N_2$) continued for an additional 30–45 min to minimize oxygen, ensuring dissolved oxygen levels remained below 5 ppb, as verified with an Orbisphere analyzer. Once the autoclave was sealed and checked for any possible leaks, in the case of $CO_2$ experiments, the pressure was increased to 3.4 MPa and the temperature was set to 150 °C. Once the target temperature was reached, high-pressure $CO_2$ sourced from a high-purity bottle was added to the autoclave, aided by a gas booster pump to achieve the total pressure of 13.8 MPa. In the case of the $N_2$ experiment, after sealing the system, the temperature was increased to 150 °C, which resulted in a total pressure of ~0.34 MPa.

In both types of experiments ($CO_2$ or $N_2$), after the target temperature and pressure were reached, the pH of the solution was checked using the HP/HT pH probe and then the open circuit potential (OCP) was monitored for ~ 1 h to ensure the stability of the system. After one hour of OCP monitoring, the LPR was conducted on the specimen by polarizing it to the potentials of ± 10 mV with respect to OCP at a scan rate of 0.125 mV/s.

We note that LPR is not quantitatively reliable for passive alloys, especially if any localized corrosion initiates. Although localized attacks are unlikely within the small polarization range used for LPR (±10 mV vs OCP), passive films can still produce non-linear behavior in this region. As a result, the measured current may reflect film charging/defect transport rather than uniform metal dissolution, and Stern–Geary estimates of corrosion current ($i_{corr}$) (Kelly et al., 2002) carry large uncertainties. Accordingly, we only use polarization resistance ($R_p$) values, obtained from LPR, primarily as qualitative/comparative indicators of passivation and film stability rather than an absolute corrosion rate. $R_p$ (ohm) was determined by the slope of the current voltage curve ($\partial E / \partial i$) at OCP.

The CPP measurement was conducted after the LPR experiment and a short period of OCP monitoring (i.e., 60 s, to ensure OCP stability). The CPP scan started at −100 mV vs. OCP, moving toward anodic potentials until reaching an apex current density of 50 $mA/m^2$, and then reversed direction until returning to the original OCP. The scan rate for the CPP experiments was 0.166 mV/s.

Cathodic polarization measurements for both 13Cr and S13Cr specimens were conducted under the same experimental conditions, as shown in Table 2 by polarizing the working electrode in the cathodic direction from OCP up to −1 V vs. OCP. Electrochemical impedance spectroscopy (EIS; 10 mV AC perturbation, 10 kHz–0.01 Hz) was used to determine the solution resistance ($R_s$), which was then applied for iR (ohmic) drop correction of the electrochemical data. All electrochemical measurements were performed in duplicate.

Samples retrieved after each electrochemical experiment were cleaned with DI water and isopropanol, then kept in a desiccator to minimize oxidation prior to further characterization.

### 2.3. Surface characterization

At the end of the electrochemical experiments, the corroded surfaces and corrosion product layers were characterized using SEM and EDS techniques. The composition of the passive layers on S13Cr, DSS, and SDSS specimens was characterized using XPS. In this case, as mentioned earlier, rectangular specimens were exposed to the same conditions as those of the electrochemical experiments (as described in Table 2) for the exposure time of 1 day. The XPS measurements were performed using a PHI Versaprobe 5000 X-ray photoelectron spectroscopy with a monochromatic Al Kα source (1486.6 eV) with a probe diameter of 200 μm and a take-off angle of 45° A pass energy of 23.5 eV was used to obtain high-resolution spectra of each characteristic peak. After acquiring the spectra, the adventitious C 1 s peak at 284.8 eV was used as a reference for charge correction. CasaXPS was used for XPS fitting and analysis.

## 3. Results

### 3.1. 13Cr

According to Fig. 2(a), 13Cr exhibits active corrosion behavior in $scCO_2$ and $N_2$ saturated NaCl solution at the same initial pH. Despite the similarities, the anodic reaction is accelerated in the $N_2$ environment compared to $scCO_2$. The corrosion rate is similar in both environments, which can be explained by a decelerated cathodic reaction in the $N_2$ environment compared to $scCO_2$, as shown in Fig. 2(b). The presence of $CO_2$ in the gas phase (or in a dense phase under $scCO_2$ conditions) results in the dissolution of $CO_2$ in water and the formation of carbonic acid ($H_2CO_3$) through hydration as follows (Nordsveen et al., 2003):

$$CO_2(aq) + H_2O(l) \rightleftharpoons H_2CO_3(aq) \quad (1)$$

Dissociation of $H_2CO_3$ produces $H^+$ ions:

$$H_2CO_3(aq) \rightleftharpoons H^+(aq) + HCO_3^-(aq) \quad (2)$$

$$HCO_3^-(aq) \rightleftharpoons H^+(aq) + CO_3^{2-}(aq) \quad (3)$$

These additional $H^+$ ions will be consumed in the hydrogen evolution reaction:

$$2H^+(aq) + 2e^- \rightarrow H_2(g) \quad (4)$$

This phenomenon, when the dissociation of a weak acid provides extra protons for the corrosion reaction, is defined as the “buffering effect” (Ayyagari et al., 2024; Kahyarian et al., 2017). According to Fig. 2(b) in the $scCO_2$ environment, due to the buffering effect, the extent of the charge-transfer controlled portion of the cathodic sweep

[1] “High Temp & High Pressure pH Electrode,” Corr Instruments, www.corrinstruments.com.

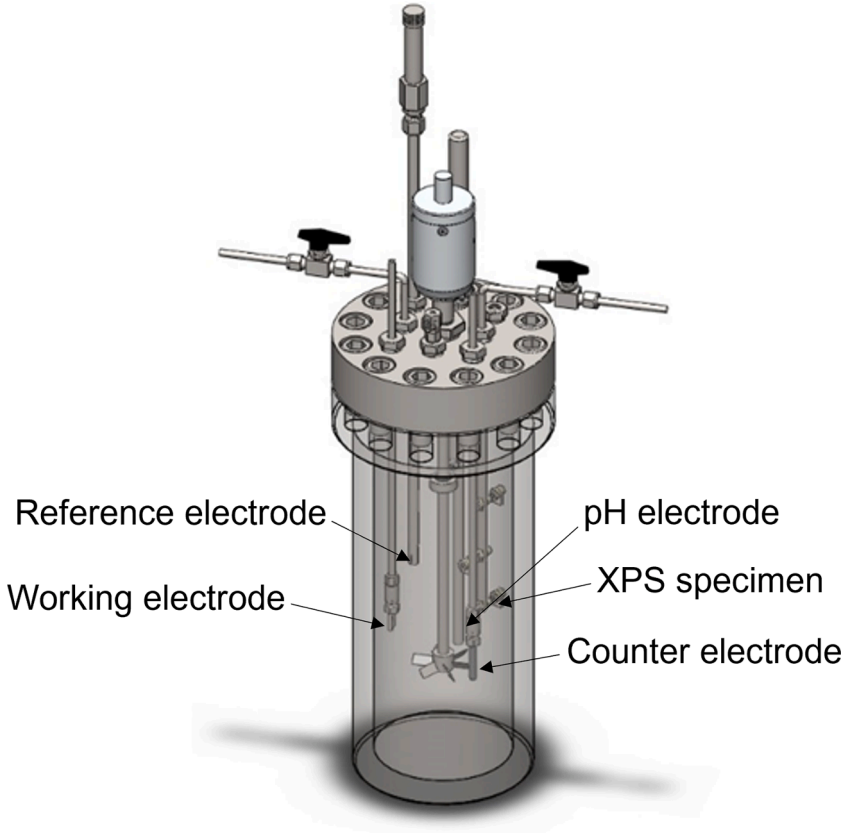


**Fig. 1.** Schematic representation of the HP/HT autoclave setup.

**Table 2**
Details of electrochemical experiments.

| Experimental variable | Content | |
|---|---|---|
| Test solution | 3 wt. % NaCl | |
| Temperature | 150 °C | |
| pH (at 150 °C) | 2.9 | |
| Working electrode material | 13Cr, S13Cr, DSS, SDSS | |
| Gas | $CO_2$ | $N_2$ |
| Total pressure | 13.8 MPa | 0.34 MPa |
| Electrochemical measurements | OCP, LPR, CPP | |

and the limiting current density are increased.

Further comparison of the corrosion behavior of 13Cr in $N_2$ vs $scCO_2$ environment was done using SEM and EDS analysis after the CPP measurements, as demonstrated in Figs. 3–5. According to Fig. 3, in the $scCO_2$ environment, the surface was covered by a layer of oxide, as evidenced by the presence of the O peak in the EDS spectra (Fig. 3(c)). The compositions of both the alloy matrix (covered by the oxide layer, Fig. 3(c)) and the localized corroded areas (Fig. 3(d)) show a higher concentration of Cr compared to Fe, which indicates active corrosion, verifying the electrochemical data recorded during the CPP experiment. The traces of the polishing line observed on the matrix suggest that the oxide layer is thin.

As illustrated in Fig. 4(a) and (b), in the $N_2$ environment, similar to the $scCO_2$ environment the areas subject to uniform corrosion and the

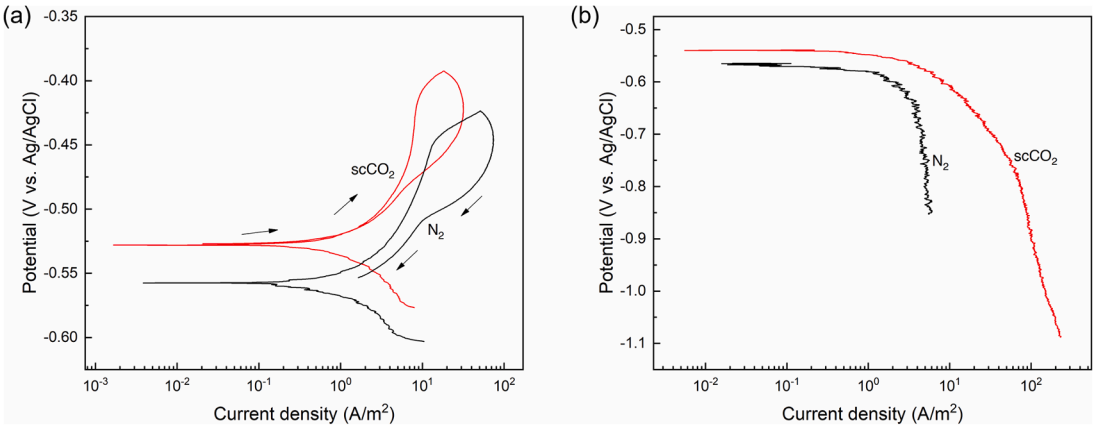


**Fig. 2.** Polarization curves of 13Cr in 3 wt. % NaCl solution under total pressure of 13.8 MPa ($scCO_2$ environment) and 0.34 MPa ($N_2$ environment) at 150 °C (a) cyclic anodic and (b) cathodic polarization.

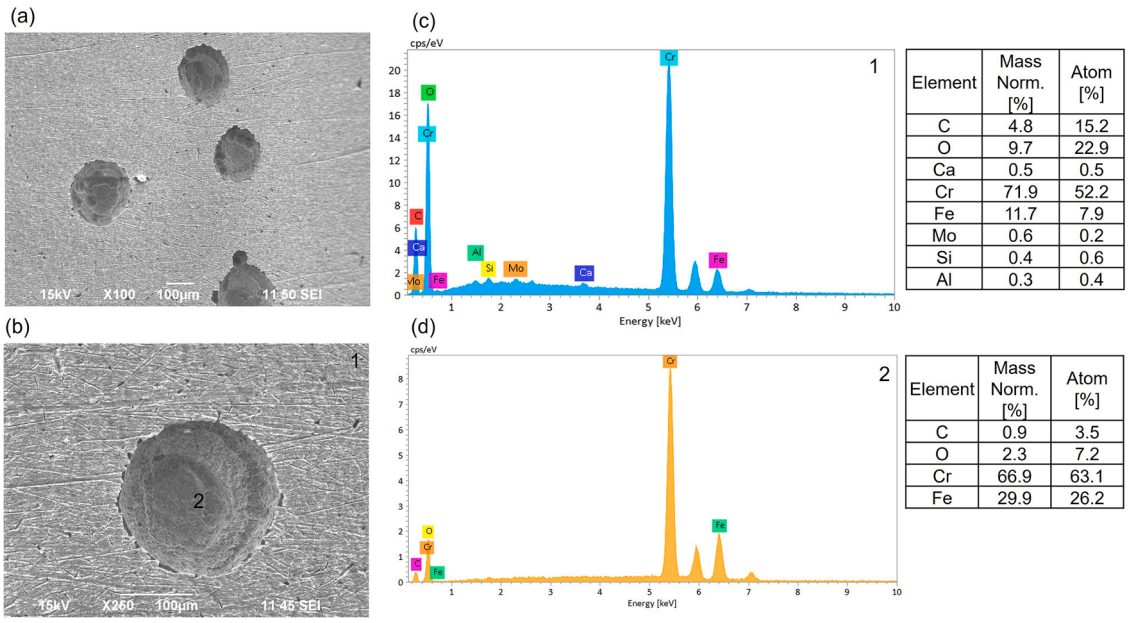


| Element | Mass Norm. [%] | Atom [%] |
|---|---|---|
| C | 4.8 | 15.2 |
| O | 9.7 | 22.9 |
| Ca | 0.5 | 0.5 |
| Cr | 71.9 | 52.2 |
| Fe | 11.7 | 7.9 |
| Mo | 0.6 | 0.2 |
| Si | 0.4 | 0.6 |
| Al | 0.3 | 0.4 |

| Element | Mass Norm. [%] | Atom [%] |
|---|---|---|
| C | 0.9 | 3.5 |
| O | 2.3 | 7.2 |
| Cr | 66.9 | 63.1 |
| Fe | 29.9 | 26.2 |

**Fig. 3.** SEM image of (a) and (b) 13Cr after CPP measurement in 3 wt. % NaCl solution under total pressure of 13.8 MPa ($scCO_2$ environment) at 150 °C and EDS analysis of the area (c) 1 and (d) 2 from Fig. 3(b).

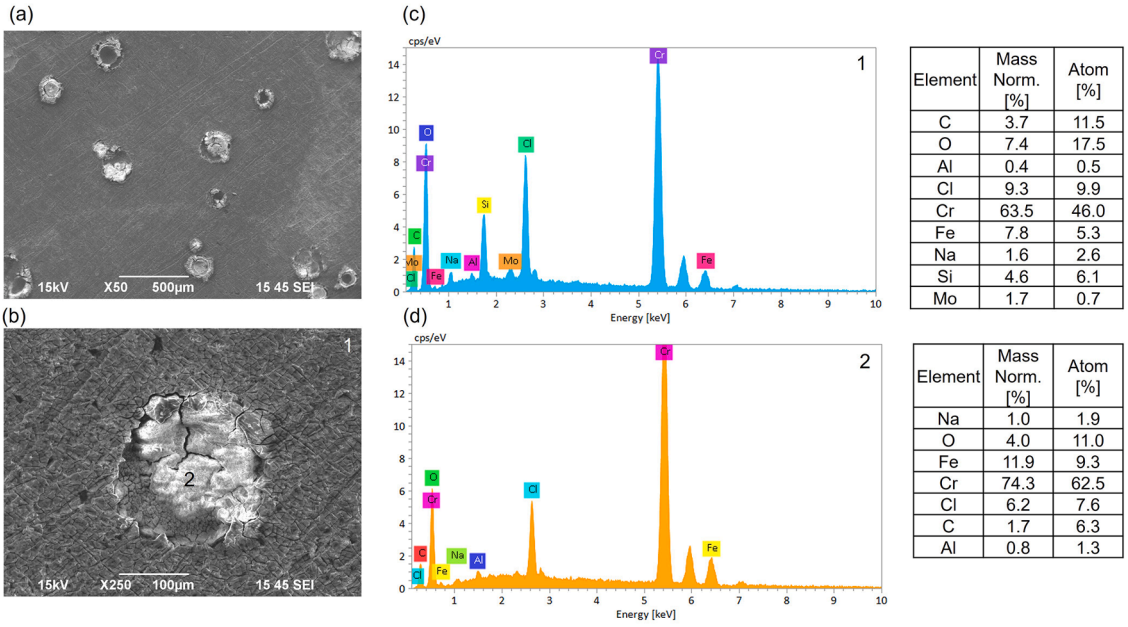


| Element | Mass Norm. [%] | Atom [%] |
|---|---|---|
| C | 3.7 | 11.5 |
| O | 7.4 | 17.5 |
| Al | 0.4 | 0.5 |
| Cl | 9.3 | 9.9 |
| Cr | 63.5 | 46.0 |
| Fe | 7.8 | 5.3 |
| Na | 1.6 | 2.6 |
| Si | 4.6 | 6.1 |
| Mo | 1.7 | 0.7 |

| Element | Mass Norm. [%] | Atom [%] |
|---|---|---|
| Na | 1.0 | 1.9 |
| O | 4.0 | 11.0 |
| Fe | 11.9 | 9.3 |
| Cr | 74.3 | 62.5 |
| Cl | 6.2 | 7.6 |
| C | 1.7 | 6.3 |
| Al | 0.8 | 1.3 |

**Fig. 4.** SEM image of (a) and (b) 13Cr after CPP measurement in 3 wt. % NaCl solution under total pressure of 0.34 MPa ($N_2$ environment) at 150 °C and EDS analysis of the area (c) 1 and (d) 2 from Fig. 4(b).

localized corroded areas are covered by a corrosion product layer. As depicted in the EDS results in Fig. 4(c) and (d), the composition of this corrosion product layer contains O, a high amount of Cr (compared to Fe), and a trace of other alloying elements such as Mo and Mn. In order to compare the morphology of the localized corroded areas in the two environments, the corrosion product layer formed in the $N_2$ environment was removed by ultrasonically cleaning the specimen in DI water. After the sonication process, as seen in Fig. 5, the uniformly corroded areas reveal a grained-like morphology that indicates a high rate of corrosion. The morphology of localized corroded areas appears to be similar in $scCO_2$ and $N_2$ environments.

### 3.2. S13Cr

S13Cr exhibits passive behavior in both $scCO_2$ and $N_2$ environments with a similar pitting potential of ~ −0.25 V vs Ag/AgCl (Fig. 6). However, the passive current density in the $N_2$ environment is slightly higher than that in the $scCO_2$ environment (~0.25 A/$m^2$ vs ~0.15 A/$m^2$). Despite the enhanced cathodic kinetics in the $scCO_2$ environment due to the "buffering effect", as shown in Fig. 6(b), the corrosion rate, dominated by the kinetics of anodic reaction, remains similar in both environments. In the reserve scan, S13Cr does not re-passivate above the OCP potential in either of the environments.

The surfaces of S13Cr specimens subjected to CPP measurements in the $scCO_2$ and $N_2$ environments were examined using SEM and EDS

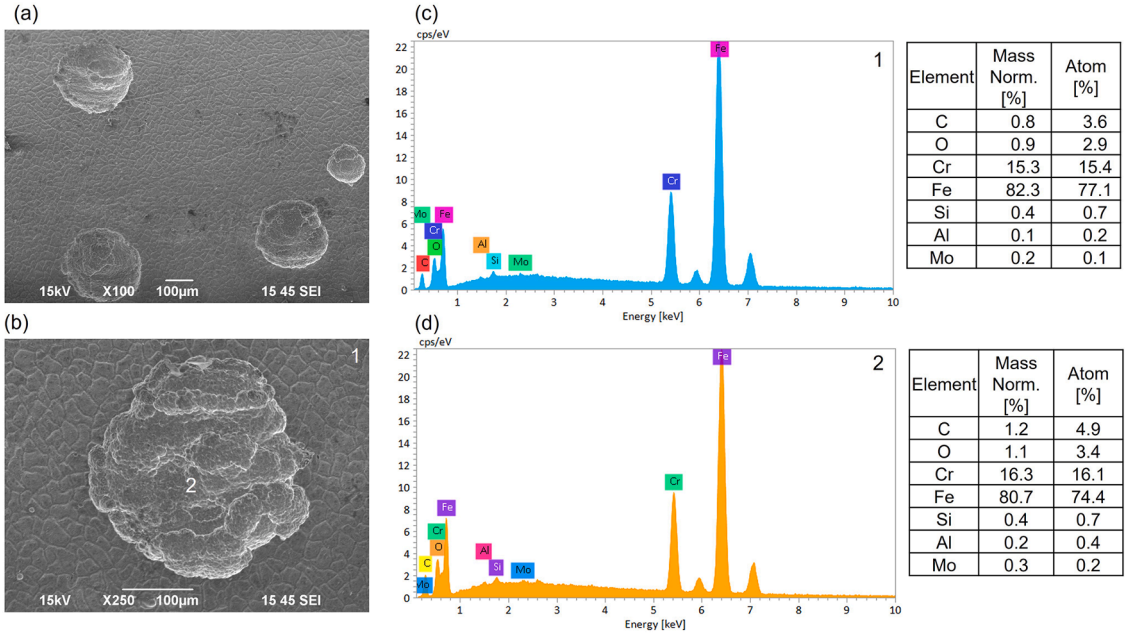


| Element | Mass Norm. [%] | Atom [%] |
|---|---|---|
| C | 0.8 | 3.6 |
| O | 0.9 | 2.9 |
| Cr | 15.3 | 15.4 |
| Fe | 82.3 | 77.1 |
| Si | 0.4 | 0.7 |
| Al | 0.1 | 0.2 |
| Mo | 0.2 | 0.1 |

| Element | Mass Norm. [%] | Atom [%] |
|---|---|---|
| C | 1.2 | 4.9 |
| O | 1.1 | 3.4 |
| Cr | 16.3 | 16.1 |
| Fe | 80.7 | 74.4 |
| Si | 0.4 | 0.7 |
| Al | 0.2 | 0.4 |
| Mo | 0.3 | 0.2 |

**Fig. 5.** SEM image of (a) and (b) ultrasonically cleaned 13Cr after CPP measurement in 3 wt. % NaCl solution under total pressure of 0.34 MPa ($N_2$ environment) at 150 °C and EDS analysis of the area (c) 1 and (d) 2 from Fig. 5(b).

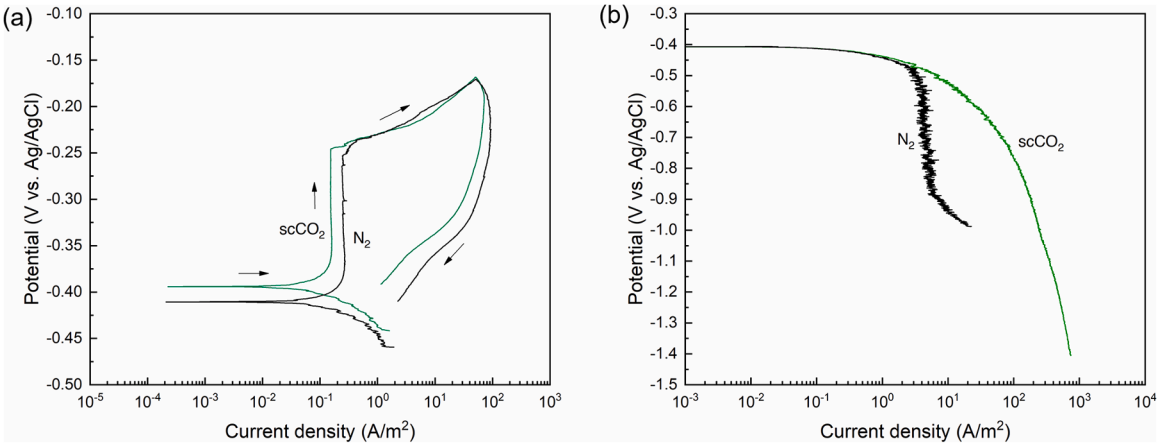


**Fig. 6.** Polarization curves of S13Cr in 3 wt. % NaCl solution under total pressure of 13.8 MPa ($scCO_2$ environment) and 0.34 MPa ($N_2$ environment) at 150 °C (a) cyclic anodic and (b) cathodic polarization.

analysis. The results are shown in Figs. 7 and 8. As it was expected from the electrochemical data, pits were found on the S13Cr surface tested in both $scCO_2$ and $N_2$ environments. The pits after the CPP measurement in the $scCO_2$ environment were covered by pit-covers (Fig. 7(a)), which were removed by ultrasonically cleaning the specimen in DI water. The composition of the passive regions on the surface matches the bulk alloy composition (Fig. 7(d)), while the composition inside the pitting (as shown in Fig. 7(e)) includes a high concentration of Cr, and a significant amount of other alloying elements such as Mo and Mn, which indicates the high rate of corrosion inside the pitting areas.

Similar corrosion morphology and composition were observed on S13Cr after the cyclic polarization experiment in the $N_2$ environment. In this case, the pits were also covered by corrosion products/pit-cover (as shown in Fig. 8(a)). Therefore, the surface was cleaned ultrasonically in DI water (Fig. 8(b) and (c)) before examining the composition of the passive and locally corroded regions. The EDS results (shown in Fig. 8(d) and (e)) are similar to those previously observed in the $scCO_2$ environment. However, further characterization of the passive films using techniques such as XPS is required to make a comparison between the behavior in the two environments.

The results of XPS analysis on the passive film formed on S13Cr in the $scCO_2$ and $N_2$ environments are shown in Fig. 9 in the form of high-resolution peaks of Cr, O, and Mo. No difference in the general composition between the passive films formed in the two environments is observed. This confirms that the passive films in both environments are composed of a combination of Cr and Mo oxide and hydroxides. According to Fig. 9(a), the ratio between $Cr_2O_3$ and $Cr(OH)_3$ is different. A typical chromium oxide layer contains an inner oxide layer and an outer hydroxide layer (Keller and Strehblow, 2004). In the $scCO_2$ environment, less $Cr_2O_3$ was detected. Considering the interaction depth of the XPS technique and the fact that the metal Fe peak was not detected in either environment, the results do not provide the composition of the entire thickness of the passive layer. Nevertheless, the passive layer thickness is likely thicker in the $scCO_2$ environment, since the detected portion was mainly the outer layer.

The high-resolution O peak in Fig. 9(b) does not indicate any significant difference between the two passive films. The Mo spectra in the two environments are clearly different, as shown in Fig. 9(c), and while a

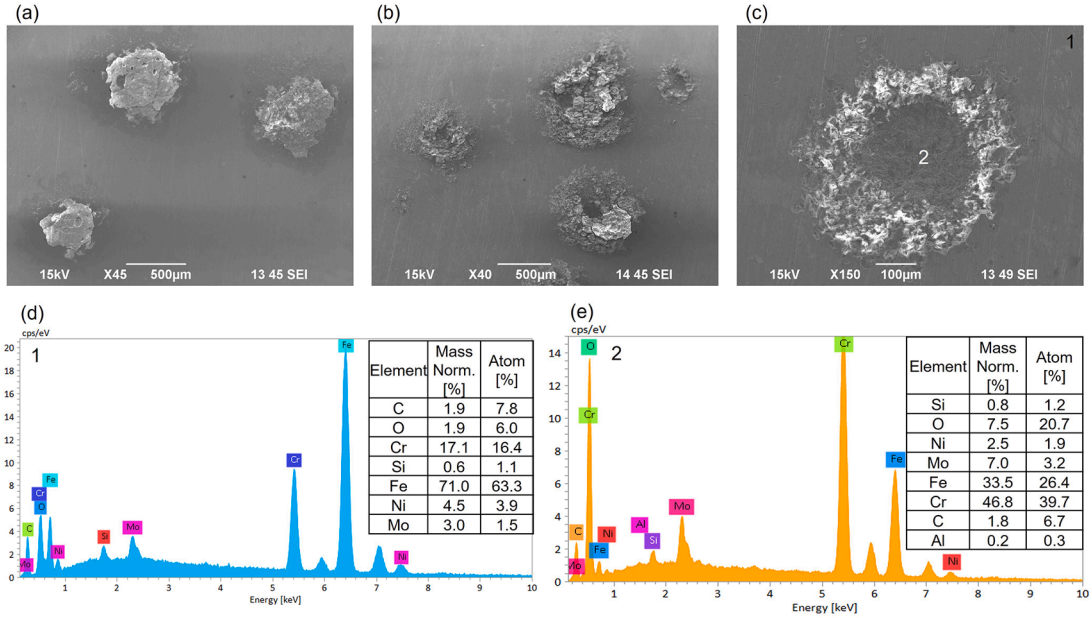


**Fig. 7.** SEM image of (a) as tested, (b) and (c) ultrasonically cleaned surface of S13Cr after CPP measurement in 3 wt. % NaCl solution under total pressure of 13.8 MPa ($scCO_2$ environment) at 150 °C and EDS analysis of the area (d) 1 and (e) 2 from Fig. 7(c).

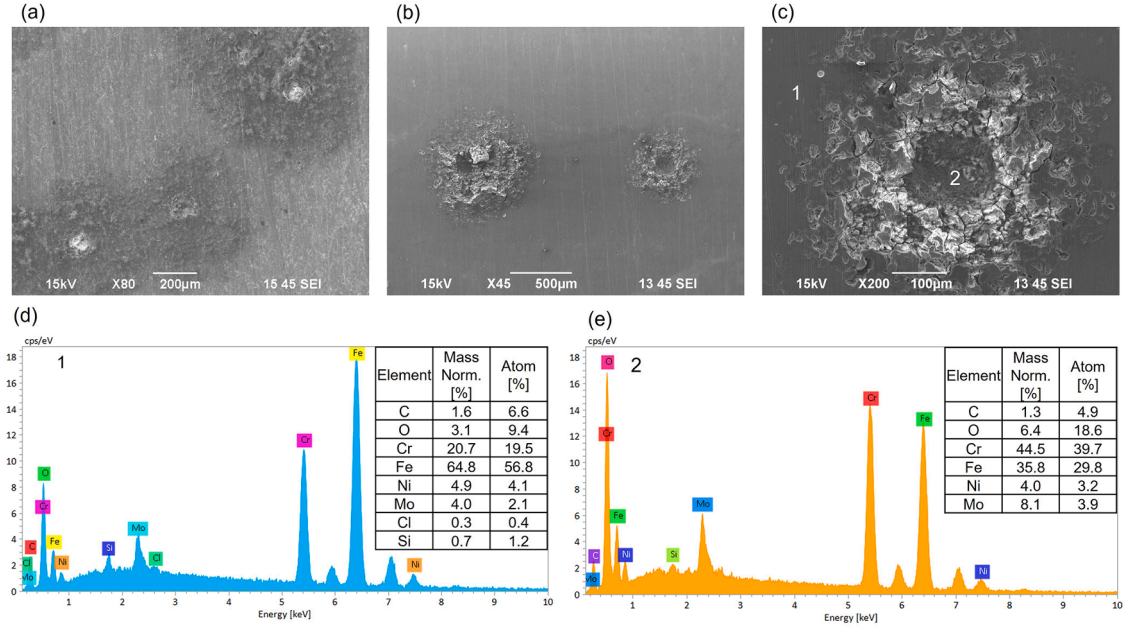


**Fig. 8.** SEM image of (a) as tested, (b) and (c) ultrasonically cleaned surface of S13Cr after cyclic polarization test in 3 wt. % NaCl solution under total pressure of 0.34 MPa ($N_2$ environment) at 150 °C and EDS analysis of the area 1 (d) and 2 (e) from Fig. 8(c).

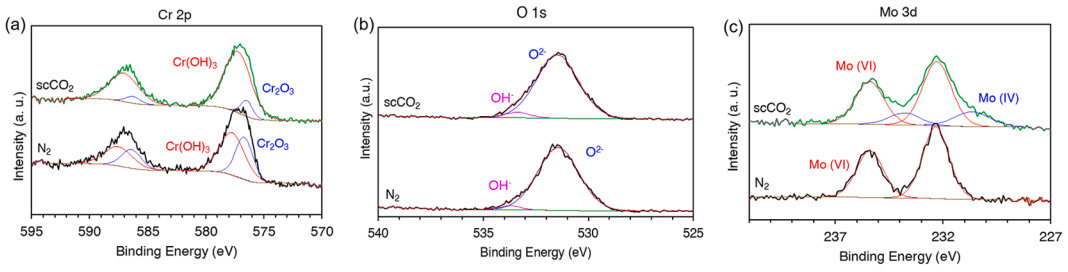


**Fig. 9.** XPS analysis of the passive layer formed on S13Cr after one day of immersion in 3 wt. % NaCl solution under total pressure of 13.8 MPa ($scCO_2$ environment) and 0.34 MPa ($N_2$ environment) at 150 °C; high resolution spectrum of (a) Cr 2p, (b) O 1 s, and (c) Mo 3d in both environments.

hint of Mo (IV) is observed at 230.7 eV for the passive film formed in the $scCO_2$ environment, the passive film formed in the $N_2$ environment contains only Mo (VI).

### 3.3. DSS (25Cr)

DSS exhibits passive behavior with a similar pitting potential (~−0.14 to −0.1 V vs Ag/AgCl) in both $scCO_2$ and $N_2$ environments (Fig. 10). The passive current densities are also comparable in both conditions. The occurrence of some metastable pitting can be observed by the current spikes in the passive region for the experiment in the $N_2$ environment. On the contrary, there are no current spikes in the passive region of the curve associated with the $scCO_2$ environment, at least not close to the pitting potential. However, as shown in Fig. 10, the current near the pitting potential in the $scCO_2$ environment displays some fluctuation, which may indicate the occurrence of metastable pitting or the onset of pitting initiation.

In the reverse scan under the $N_2$ environment, DSS re-passivates at ~−0.3 V vs Ag/AgCl, which is ~100 mV more noble than its original OCP value (~−0.4 V vs Ag/AgCl). Interestingly, as shown in Fig. 10, DSS does not re-passivate at potentials above its original OCP in the $scCO_2$ environment. In both cases, DSS shows positive hysteresis during the reverse scan, meaning that the value of current density is higher than that observed in the forward scan at the same potential. However, in the $N_2$ environment, the current density significantly decreases with decreasing potential, which finally leads to re-passivation. In the $scCO_2$ environment, the decrease in the current density with decreasing the potential is significantly slower, when compared to the $N_2$ environment, and even at OCP, the value of current density in the reverse scan is one order of magnitude higher than the value during the forward scan. The high value of current density in the $scCO_2$ environment could indicate the propagation of pitting on the surface.

It is noticeable that the corrosion current is similar in the two experiments, which is due to the dominating effect of the anodic reaction, that is, as previously mentioned, similar in $N_2$ and $scCO_2$ environments.

After the CPP experiment in the $scCO_2$ environment, as shown in the SEM image in relatively low magnification (Fig. 11(a)), several areas of localized corrosion were observed on the surface of the specimen. The SEM image at a higher magnification of one of these areas (shown in Fig. 11(b)) suggests that these areas could be individual pits that propagated and connected during the reverse scan. The high current density that was observed during the reverse scan for this experiment (red curve in Fig. 10) corroborates this observation.

The chemical composition of the passive and localized corrosion areas (shown as areas 1 and 2 in Fig. 11(b)) are provided in Fig. 11(c) and (d), respectively. The composition in the center of the localized corrosion area includes a higher amount of Cr and other alloying elements e.g., Mo, Ni, etc., compared to the composition of the passive area, which also suggests the high rate of anodic dissolution of Fe.

The surface of the specimen after the CPP experiment in $N_2$ environment shows the presence of several individual pits (Fig. 12(a) and (b)). The presence of these pits that are not as propagated as those previously observed on the surface of the specimen exposed to the $scCO_2$ environment (Fig. 11(b)) agrees with the re-passivation behavior during the reverse scan (black curve in Fig. 10).

The chemical composition of the passive area (area 1, shown in Fig. 12(c)) is close to the bulk composition of the alloy, while the composition at the center of the pit (area 2, shown in Fig. 12(d)) contains a higher fraction of Cr, which is due to the high Fe dissolution rate inside this localized corrosion area.

The XPS results of the DSS passive films formed in $scCO_2$ and $N_2$ environments are shown in Fig. 13. In this figure, the high-resolution spectra of Cr (Fig. 13(a)) and Mo (Fig. 13(b)) of passive films are compared in the two environments. No difference in Cr spectra of the films are observed (Fig. 13(a)). However, in the Mo spectrum, some changes in the ratio of Mo (IV)/Mo (VI) can be seen for the films formed in two different environments (Fig. 13(b)).

### 3.4. SDSS (2507)

As shown in Fig. 15, SDSS exhibits passive behavior in both $scCO_2$ and $N_2$ environments with a similar pitting potential of ~ 0.05 V vs Ag/AgCl. The passive current densities are also quite similar in both environments. However, within the passive region, the frequency and the amplitude of current spikes related to the formation of metastable pitting are higher in the $N_2$ environment than in the $scCO_2$ environment.

During the reverse scan, SDSS presents notable differences in behavior between the $scCO_2$ and $N_2$ environments. While this alloy

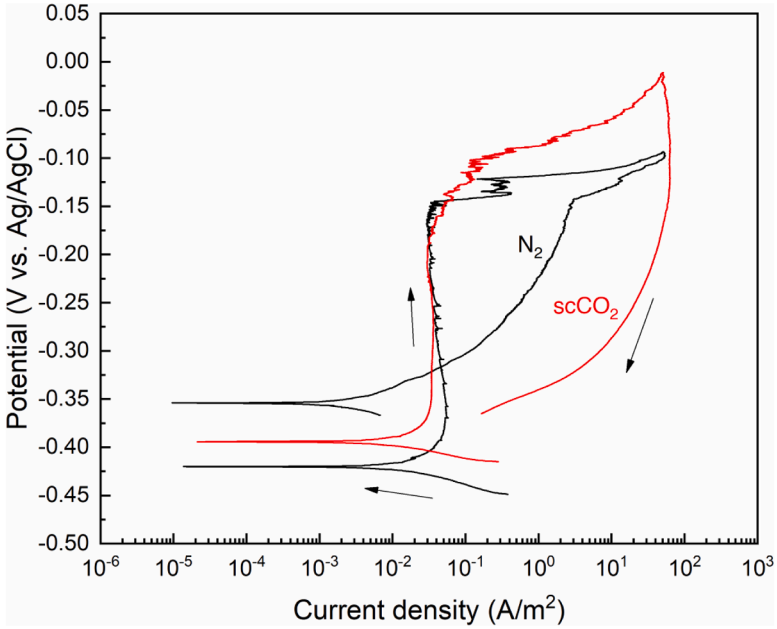


**Fig. 10.** Cyclic polarization curves of DSS (25Cr) in 3 wt. % NaCl solution under total pressure of 13.8 MPa ($scCO_2$ environment) and 0.34 MPa ($N_2$ environment) at 150 °C.

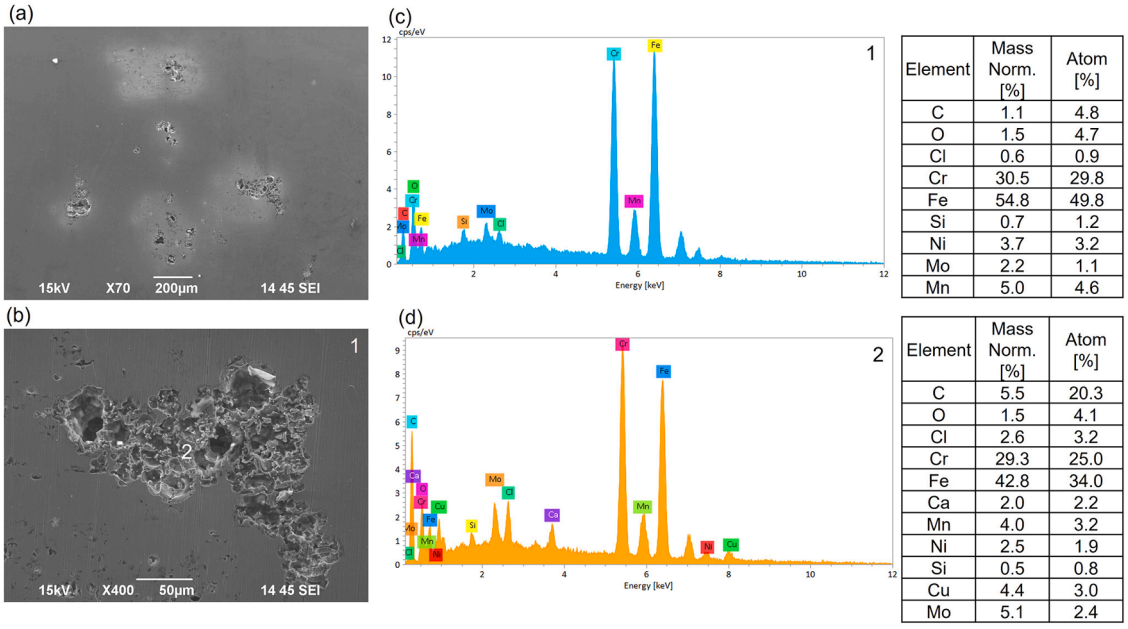


| Element | Mass Norm. [%] | Atom [%] |
|---|---|---|
| C | 1.1 | 4.8 |
| O | 1.5 | 4.7 |
| Cl | 0.6 | 0.9 |
| Cr | 30.5 | 29.8 |
| Fe | 54.8 | 49.8 |
| Si | 0.7 | 1.2 |
| Ni | 3.7 | 3.2 |
| Mo | 2.2 | 1.1 |
| Mn | 5.0 | 4.6 |

| Element | Mass Norm. [%] | Atom [%] |
|---|---|---|
| C | 5.5 | 20.3 |
| O | 1.5 | 4.1 |
| Cl | 2.6 | 3.2 |
| Cr | 29.3 | 25.0 |
| Fe | 42.8 | 34.0 |
| Ca | 2.0 | 2.2 |
| Mn | 4.0 | 3.2 |
| Ni | 2.5 | 1.9 |
| Si | 0.5 | 0.8 |
| Cu | 4.4 | 3.0 |
| Mo | 5.1 | 2.4 |

**Fig. 11.** SEM image of (a) and (b) DSS (25Cr) after CPP measurement in 3 wt. % NaCl solution under total pressure of 13.8 MPa ($scCO_2$ environment) at 150 °C and EDS analysis of the area (c) 1 and (d) 2 from Fig. 11(b).

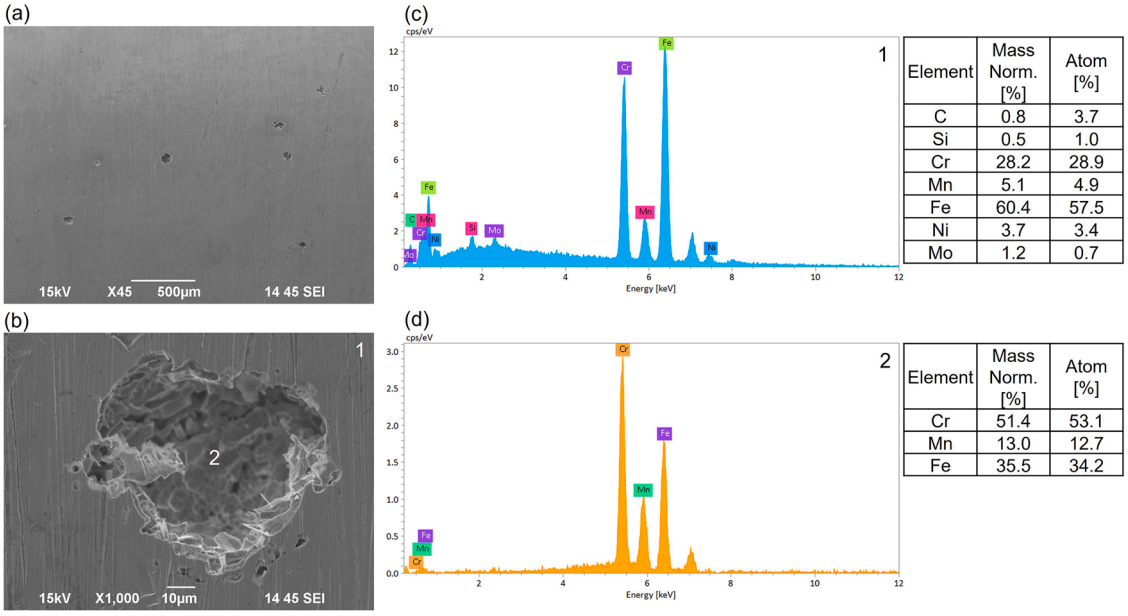


| Element | Mass Norm. [%] | Atom [%] |
|---|---|---|
| C | 0.8 | 3.7 |
| Si | 0.5 | 1.0 |
| Cr | 28.2 | 28.9 |
| Mn | 5.1 | 4.9 |
| Fe | 60.4 | 57.5 |
| Ni | 3.7 | 3.4 |
| Mo | 1.2 | 0.7 |

| Element | Mass Norm. [%] | Atom [%] |
|---|---|---|
| Cr | 51.4 | 53.1 |
| Mn | 13.0 | 12.7 |
| Fe | 35.5 | 34.2 |

**Fig. 12.** SEM image of (a) and (b) DSS (25Cr) after CPP measurement in 3 wt. % NaCl solution under total pressure of 0.34 MPa ($N_2$ environment) at 150 °C and EDS analysis of the area (c) 1 and (d) 2 from Fig. 12(b).

apparently re-passivates in both environments, the re-passivation potential in the $N_2$ environment is ~ 150 mV more noble than in the $scCO_2$ environment: ~ −0.15 V vs Ag/AgCl in $N_2$ and ~ −0.3 V vs Ag/AgCl in $scCO_2$. In both environments, a positive hysteresis during the reverse scan is observed; however, the hysteresis loop in the $N_2$ environment is smaller, and the current density decreases more rapidly with decreasing potential compared to the $scCO_2$ environment. As a result, in the $N_2$ environment, re-passivation occurs at a potential only ~100 mV below the pitting potential and ~250 mV above the original OCP.

In the $scCO_2$ environment, after pitting has occurred, a drastic change in the slope of the current/potential curve at ~ 0.1 V vs Ag/AgCl is observed, which could be attributed to a change in the mode of corrosion. As a result of this change of slope, the polarization had to be continued up to 0.5 V vs Ag/AgCl to reach the apex current of 50 $A/m^2$, as compared to reaching the apex current at 0.17 V vs Ag/AgCl in $N_2$ environment. In addition, or possibly as a direct result of this behavior, the difference in the current density during the reverse and forward scan is quite significant. For example, this difference in the original passive region's potential range is three orders of magnitude. Therefore, as observed in Fig. 14, the accumulative current passed through the specimen during the reverse scan is greater in $scCO_2$ compared to that in the $N_2$ environment. In the $scCO_2$ environment, re-passivation occurs only ~100 mV above the original OCP.

Similar to what was observed for DSS, the corrosion current seems similar for SDSS in both environments, which is due to the dominating influence of the anodic reaction kinetics that are similar in $scCO_2$ and $N_2$

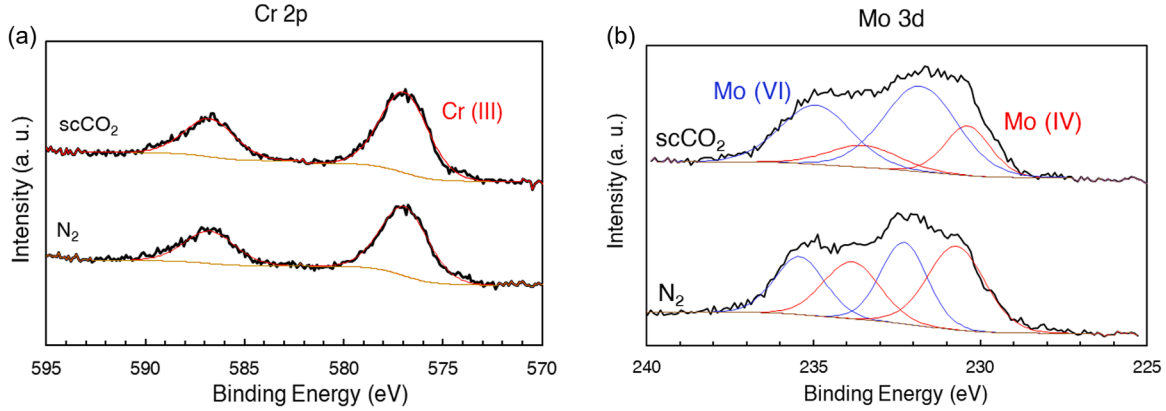


**Fig. 13.** XPS analysis of the passive layer formed on DSS (25Cr) after one day of immersion in 3 wt. % NaCl solution under total pressure of 13.8 MPa ($scCO_2$ environment) and 0.34 MPa ($N_2$ environment) at 150 °C; high resolution spectrum of (a) Cr 2p and (b) Mo 3d in both environments.

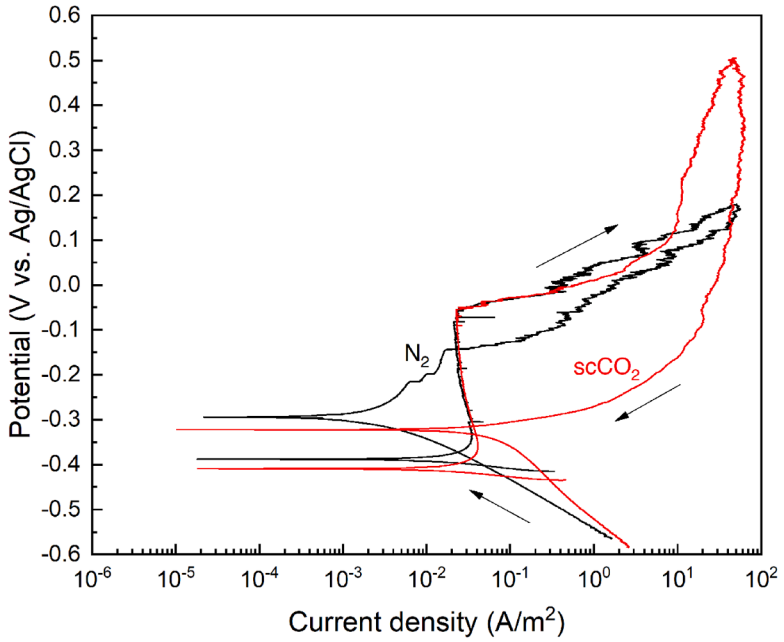


**Fig. 14.** Cyclic polarization curves of SDSS (2507) in 3 wt. % NaCl solution under total pressure of 13.8 MPa ($scCO_2$ environment) and 0.34 MPa ($N_2$ environment) at 150 °C.

in this case as well.

As previously mentioned in the experimental procedure, the edge of each specimen from the connection point to the shaft was covered by a thin layer of Xylon coating to avoid the occurrence of crevice corrosion. It is important to note that due to the severity of the conditions of the experiment, the options to prevent this type of corrosion were limited. We examined the edge of specimens using SEM after each CPP experiment to ensure that the results presented were not affected by crevice corrosion. However, as shown in Fig. 15(b), for SDSS in the $scCO_2$ environment, the occurrence of crevice corrosion was inevitable. On the surface of this specimen, after the experiment in the $scCO_2$ environment, a few propagated pits were observed as well (Fig. 15(a)). In this case, similar to the surface of DSS after the CPP experiment in the $scCO_2$ environment (Fig. 11(b)), it seems that individual pits have connected together. However, the extent of propagation seems limited on SDSS when compared to DSS, possibly due to earlier re-passivation. Fig. 15 includes the results of EDS analysis on the passive (area 1 in Fig. 15(a)) and pitting (area 2 in Fig. 15(a)). While according to Fig. 15(c), the composition in the non-corroded passive area is close to the bulk chemical composition of the alloy, the composition inside the pits (Fig. 15(d) shows a significantly higher concentration of Cr and Mo, which is due to the high rate of Fe dissolution in this area.

It is noted that the occurrence of crevice corrosion under $scCO_2$ can cause uncertainty in the polarization data (Fig. 14), including a sharp increase in current at potentials lower than expected for pitting, as well as poor reproducibility. However, the CPP measurements were repeated several times to minimize the latter issue. It can also cause apparent re-passivation in the reverse scan due to local film breakdown and subsequent re-passivation inside the crevice, making the comparisons between the two environments more challenging.

After the CPP experiment in the $N_2$ environment, the surface of the SDSS specimen shows the occurrence of pitting corrosion, as depicted in Fig. 16(a). According to this figure, pits appear to be individually located. The chemical composition of the passive area (shown in Fig. 16 (c)) is close to the bulk composition of SDSS, while the center of the pit shows a higher percentage of chromium (Fig. 16(d)). The difference in the composition between the passive area and the pitting is not as significant as what was previously observed for SDSS in the $scCO_2$

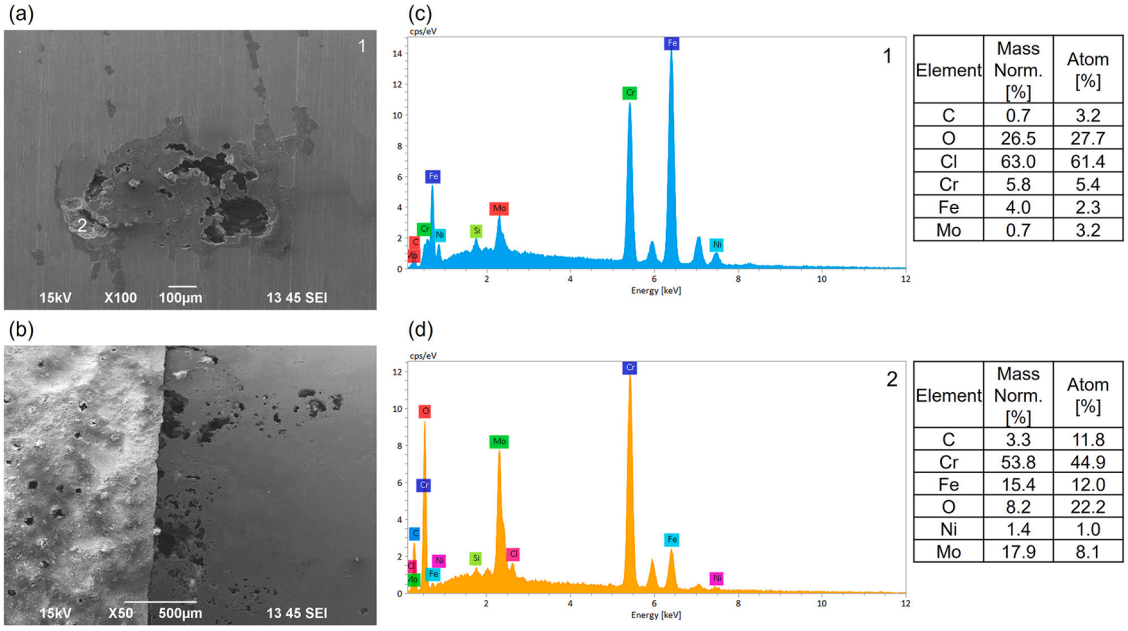


| Element | Mass Norm. [%] | Atom [%] |
|---|---|---|
| C | 0.7 | 3.2 |
| O | 26.5 | 27.7 |
| Cl | 63.0 | 61.4 |
| Cr | 5.8 | 5.4 |
| Fe | 4.0 | 2.3 |
| Mo | 0.7 | 3.2 |

| Element | Mass Norm. [%] | Atom [%] |
|---|---|---|
| C | 3.3 | 11.8 |
| Cr | 53.8 | 44.9 |
| Fe | 15.4 | 12.0 |
| O | 8.2 | 22.2 |
| Ni | 1.4 | 1.0 |
| Mo | 17.9 | 8.1 |

**Fig. 15.** SEM image of (a) and (b) SDSS (2507) after CPP measurement in 3 wt. % NaCl solution under total pressure of 13.8 MPa ($scCO_2$ environment) at 150 °C and EDS analysis of the area (c) 1 and (d) 2 from Fig. 15(a).

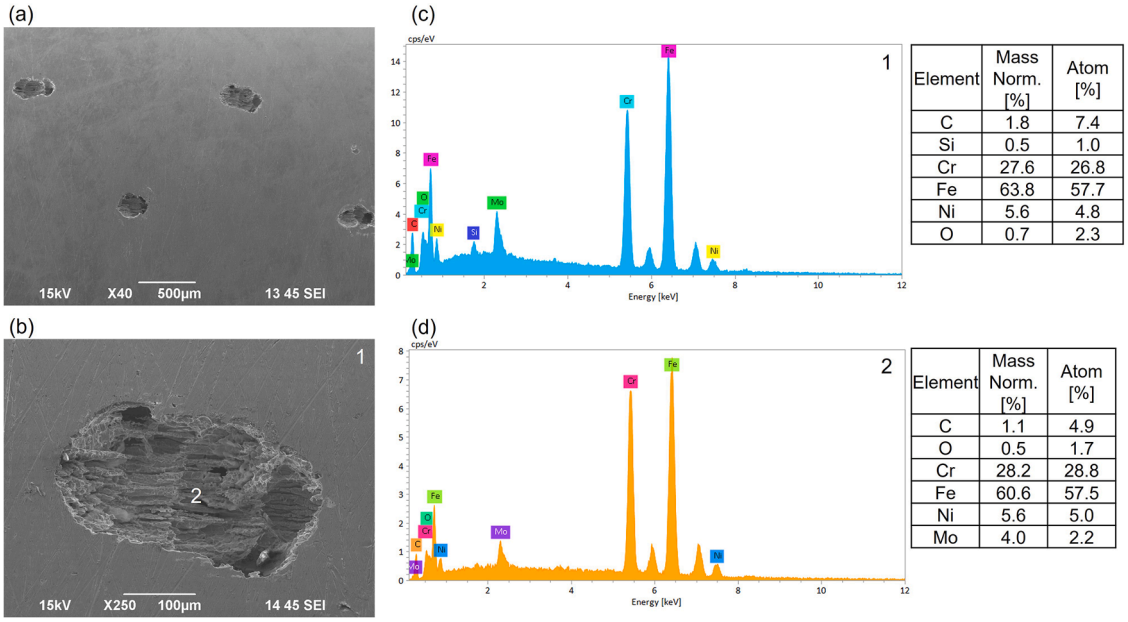


| Element | Mass Norm. [%] | Atom [%] |
|---|---|---|
| C | 1.8 | 7.4 |
| Si | 0.5 | 1.0 |
| Cr | 27.6 | 26.8 |
| Fe | 63.8 | 57.7 |
| Ni | 5.6 | 4.8 |
| O | 0.7 | 2.3 |

| Element | Mass Norm. [%] | Atom [%] |
|---|---|---|
| C | 1.1 | 4.9 |
| O | 0.5 | 1.7 |
| Cr | 28.2 | 28.8 |
| Fe | 60.6 | 57.5 |
| Ni | 5.6 | 5.0 |
| Mo | 4.0 | 2.2 |

**Fig. 16.** SEM image of (a) and (b) SDSS (2507) after CPP measurement in 3 wt. % NaCl solution under total pressure of 0.34 MPa ($N_2$ environment) at 150 °C and EDS analysis of the area (c) 1 and (d) 2 from Fig. 16(b).

environment (Fig. 15(c) and (d)) and for DSS under similar conditions in the $N_2$ environment (Fig. 12(c) and (d)).

The compositions of the passive films formed on SDSS in $scCO_2$ and $N_2$ environments examined using XPS, are shown in Fig. 17. As shown in this figure, the high-resolution spectra of Cr and Mo of the passive films formed on SDSS in $scCO_2$ and $N_2$ environments are very similar.

## 4. Discussion

The pH, particularly the surface pH, plays a critical role in the stability of the passive film formed on CRAs. The de-passivation pH refers to the threshold pH below which the passive layer, primarily composed of chromium oxide, becomes unstable and begins to degrade, increasing the material's susceptibility to corrosion. CRAs exhibit excellent corrosion resistance due to this thin, adherent passive film; however the de-passivation pH varies depending on the alloy composition, grade, and environmental conditions When the pH of the surrounding environment falls below this critical value, the passive film may dissolve or break down, compromising the alloy's corrosion resistance and promoting localized corrosion mechanisms such as pitting, crevice corrosion, or even uniform corrosion.

Upon the occurrence of localized corrosion, two main ions are introduced into the solution: $Fe^{2+}$ and $Cr^{3+}$. Let's consider the solution near the surface; the increase in concentration of $Fe^{2+}$ can increase the pH of the solution to maintain charge neutrality (Nordsveen et al., 2003). $Cr^{3+}$, on the other hand, can decrease the pH through its

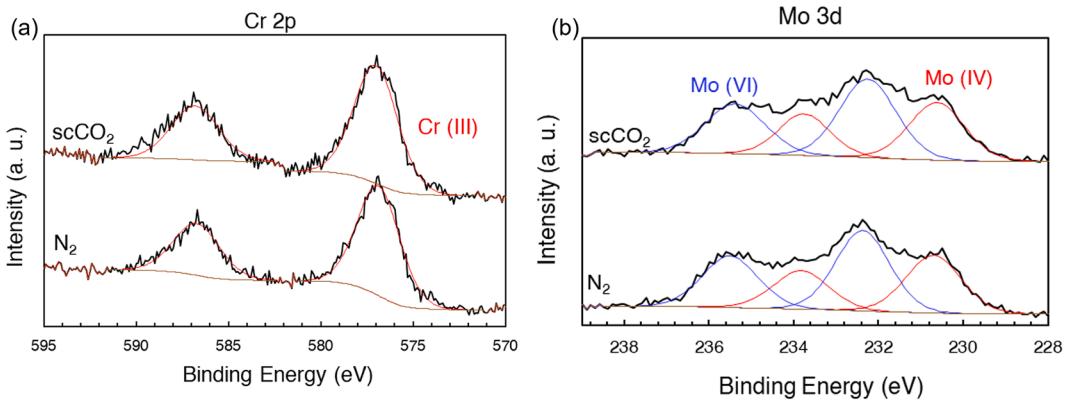


**Fig. 17.** XPS analysis of the passive layer formed on SDSS (2507) after one day of immersion in 3 wt. % NaCl solution under total pressure of 13.8 MPa ($scCO_2$ environment) and 0.34 MPa ($N_2$ environment) at 150 °C; high resolution spectrum of (a) Cr 2p and (b) Mo 3d in both environments.

hydrolysis reaction as follows (Zhang et al., 2024):

$$Cr^{3+} + 3H_2O \rightarrow Cr(OH)_3 + 3H^+ \quad (5)$$

In saturated $CO_2$ solutions, $CO_2$ dissolves to form $H_2CO_3$, which dissociates through multiple equilibria (see reactions 3 to 5). A local pH drop due to $Cr^{3+}$ hydrolysis can shift the $H_2CO_3$ dissociation reactions to the left, thereby buffering the pH to higher values. This buffering effect suggests that a $CO_2$-containing environment may be more favorable for reducing the risk of pitting corrosion in CRAs. This hypothesis is supported by observations for S13Cr, as shown in Fig. 6. Specifically, the passive current density of the S13Cr alloy in the $N_2$ environment is slightly higher than that in the $scCO_2$ environment. Moreover, metastable pitting, indicated by current spikes observed in Fig. 18(b), is present only in the $N_2$ environment.

A similar trend is observed for DSS and SDSS. As seen in Fig. 18 and Table 3, both alloys exhibit higher polarization resistance in both $N_2$ and $scCO_2$ environments compared to 13Cr and S13Cr, implying lower $Cr^{3+}$ release and hence less hydrolysis-induced acidification. Passive current densities are similar across $scCO_2$ and $N_2$, but metastable pitting spikes are again found only in the $N_2$ environment.

Despite comparable passive region behavior, DSS and SDSS show different responses after localized corrosion. Re-passivation potentials are lower in the $scCO_2$ environment for both alloys, indicating more difficult film recovery. Reverse polarization scans confirm higher current densities in the $scCO_2$ environment, consistent with propagation of localized corrosion.

Interestingly, as the post characterization with SEM shows (Fig. 15) the likelihood of crevice corrosion is higher in the $scCO_2$ environment and for the material with a higher corrosion resistance (SDSS). It is important to note that stringent measures were implemented to minimize crevice corrosion and ensure the reliability of the results. The best possible method to avoid crevice corrosion in such a harsh environment was selected and each experiment was repeated. Despite these precautions, crevice corrosion consistently occurred on SDSS in the $scCO_2$ environment, whereas no such corrosion was observed for SDSS in the $N_2$ environment or for DSS in either condition. This observation suggests a material-environment interaction specific to SDSS under $scCO_2$ exposure that facilitates crevice corrosion initiation and propagation.

DSS exhibits distinct pitting morphologies: in the $scCO_2$ environment, pits are fewer, larger, and interconnected; in the $N_2$ environment, they are smaller, more numerous, and isolated. This morphology indicates that the passive film formed in the $scCO_2$ environment possibly has fewer weak points. For SDSS, corrosion initiates at weak points such as the Xylon-coated edges, where crevice corrosion dominates due to the

**Table 3**
Values of polarization resistance ($R_p$) for different materials tested in $scCO_2$ and $N_2$ environments.

| Material | $R_p$ in $scCO_2$ environment (ohm $cm^2$) | $R_p$ in $N_2$ environment (ohm $cm^2$) |
|---|---|---|
| 13Cr | 79.7 | 73.9 |
| S13Cr | 890.8 | 539.4 |
| DSS | 5029.2 | 2634.0 |
| SDSS | 3582.5 | 3889.5 |

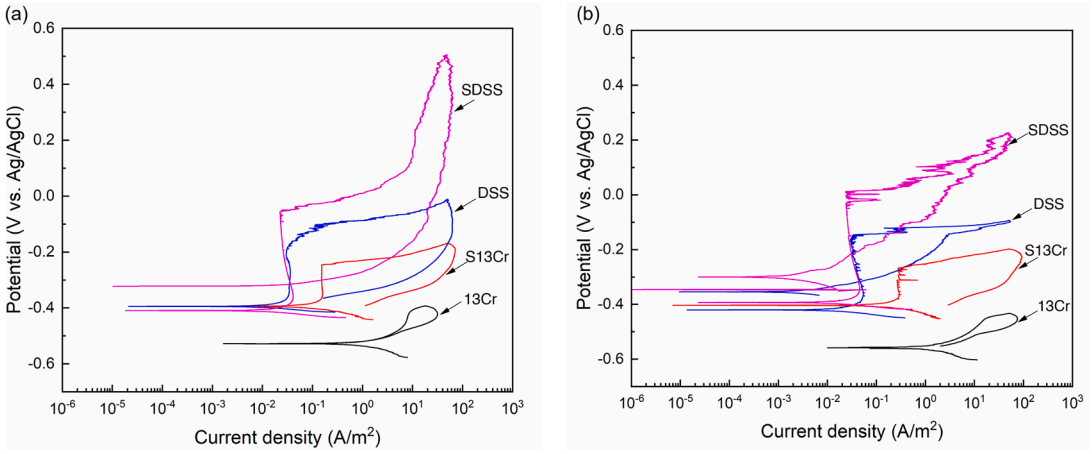


**Fig. 18.** Cyclic polarization curves of SDSS (2507), DSS (25Cr), S13Cr, and 13Cr in 3 wt. % NaCl solution under total pressure of (a) 13.8 MPa ($scCO_2$ environment) and (b) 0.34 MPa ($N_2$ environment) at 150 °C.

otherwise high firm resistance. The reverse scan response further supports these findings. In the $scCO_2$ environment, higher current densities arise from propagation of larger corrosion features, making re-passivation harder and lowering re-passivation potential.

## 5. Conclusions

The following conclusions can be drawn from this study:

- 13Cr shows active corrosion behavior under the testing conditions (3 wt. % NaCl solution, pH 2.9 at 150 °C) in both $N_2$ and $scCO_2$ environments.
- S13Cr demonstrates a typical passive behavior but without showing a re-passivation under the testing conditions in either $N_2$ or $scCO_2$ environment.
- The presence of $CO_2$ increases cathodic current density for both 13Cr and S13Cr, likely due to its buffering effect in local pH.
- DSS and SDSS show passive behavior and superior corrosion resistance under all tested conditions in both $N_2$ and $scCO_2$ environments.
- In the reserve scan, DSS and SDSS show re-passivation behavior in both environments; however, the re-passivation potential is more positive in the $N_2$ environment, suggesting easier film recovery.
- No significant compositional differences were observed in the passive films formed on S13Cr, DSS, and SDSS between $N_2$ and $scCO_2$ environments.
- Although some differences are observed, such as metastable pitting (observed as transient current spikes in the passive region in the $N_2$ environment) and variations in pit morphology, the passive films formed in $scCO_2$ and $N_2$ environments exhibit similar behavior during the forward scan of the CPP tests, indicating comparable general passivity. However, during the reverse scans, the $scCO_2$-exposed DSS and SDSS samples show more interconnected pits and crevice corrosion, repectively. These localized features lead to lower repassivation potentials and higher reverse currents, reflecting the film's limited ability to rapidly repair once locally disrupted, particularly in geometrically constrained areas where local chemistry can deviate significantly from the bulk environment. Additional work focused on localized chemistry and film repair mechanisms would further clarify these differences.

## CRediT authorship contribution statement

**Maryam Eslami:** Writing – review & editing, Writing – original draft, Methodology, Investigation, Formal analysis, Data curation, Conceptualization. **Xi Wang:** Methodology, Formal analysis, Data curation, Conceptualization. **Yoon-Seok Choi:** Writing – review & editing, Supervision, Funding acquisition, Formal analysis, Conceptualization.

## Declaration of competing interest

The authors declare that they have no known competing financial interests or personal relationships that could have appeared to influence the work reported in this paper.

## Acknowledgements

X-ray photoelectron spectroscopy was performed by Dr. Andrew Knoll in Surface and Optical Analysis Facility at the University of Akron and Dr. John Kim Swagelok Center for Surface Analysis of Materials at Case Western Reserve University.

## Data availability

Data will be made available on request.

## References

Ayyagari, S., Eslami, M., Sani, F.M., Choi, Y.S., Brown, B., Nesic, S., 2024. Effect of formic acid on aqueous corrosion mechanisms of mild steel. Electrochim. Acta 503, 144863.
Choi, Y.S., Nesic, S., Young, D., 2010. Effect of impurities on the corrosion behavior of CO2 transmission pipeline steel in supercritical CO2−water environments. Environ. Sci. Technol. 44, 9233–9238.
Cui, G., Yang, Z., Liu, J., Li, Z., 2019. A comprehensive review of metal corrosion in a supercritical CO2 environment. Int. J. Greenh. Gas Control 90, 102814.
Eslami, M., Choi, Y.S., Nesic, S., Breining, R., 2024a. Effect of formic acid (HCOOH) on the corrosion protectiveness of magnetite (Fe3O4) at elevated temperature. Corros. Sci. 229, 111868.
Eslami, M., Pan, M., Young, D., Singer, M., 2024b. Corrosion at top-of-the-line in high pressure and dense CO2 environments. Corrosion 80, 998–1012.
Haugan, E.B., Næss, M., Rodriguez, C.T., Johnsen, R., Iannuzzi, M., 2016. Effect of tungsten on the pitting and crevice corrosion resistance of type 25Cr super duplex stainless steels. Corrosion 73, 53–67.
Herzog, H., 2009. Carbon dioxide capture and storage. In: Helm, D., Hepburn, C. (Eds.), The Economics and Politics of Climate Change. Oxford University Press, p. 0.
Hua, Y., Barker, R., Neville, A., 2015. The effect of O2 content on the corrosion behaviour of X65 and 5Cr in water-containing supercritical CO2 environments. Appl. Surf. Sci. 356, 499–511.
Hua, Y., Jonnalagadda, R., Zhang, L., Neville, A., Barker, R., 2017. Assessment of general and localized corrosion behavior of X65 and 13Cr steels in water-saturated supercritical CO2 environments with SO2/O2. Int. J. Greenh. Gas Control 64, 126–136.
Hua, Y., Mohammed, S., Barker, R., Neville, A., 2020. Comparisons of corrosion behaviour for X65 and low Cr steels in high pressure CO2-saturated brine. J. Mater. Sci. Technol. 41, 21–32.
Kahyarian, A., Schumaker, A., Brown, B., Nesic, S., 2017. Acidic corrosion of mild steel in the presence of acetic acid: mechanism and prediction. Electrochim. Acta 258, 639–652.
Kairy, S.K., Zhou, S., Turnbull, A., Hinds, G., 2023. Corrosion of pipeline steel in dense phase CO2 containing impurities: a critical review of test methodologies. Corros. Sci. 214, 110986.
Keller, P., Strehblow, H.H., 2004. XPS investigations of electrochemically formed passive layers on Fe/Cr-alloys in 0.5 M H2SO4. Corros. Sci. 46, 1939–1952.
Kelly, R.G., Scully, J.R., Shoesmith, D., Buchheit, R.G., 2002. Electrochemical Techniques in Corrosion Science and Engineering. CRC Press.
Leung, D.Y.C., Caramanna, G., Maroto-Valer, M.M., 2014. An overview of current status of carbon dioxide capture and storage technologies. Renew. Sustain. Energy Rev. 39, 426–443.
Li, C., Xiang, Y., Li, W., 2019. Initial corrosion mechanism for API 5L X80 steel in CO2/SO2-saturated aqueous solution within a CCUS system: inhibition effect of SO2 impurity. Electrochim. Acta 321, 134663.
Li, K., Zhu, Z., Xiao, B., Luo, J.L., Zhang, N., 2023. State of the art overview material degradation in high-temperature supercritical CO2 environments. Prog. Mater. Sci. 136, 101107.
Li, Y., Wang, Z., Zhao, M., Zhang, G., 2018. Passivity of 13Cr stainless steel in 1% NaCl solution under dynamic supercritical CO2 conditions. Ind. Eng. Chem. Res. 57, 8718–8728.
Liu, H., Sun, J., Qian, J., Wang, B., Shi, S., Zhu, Y., Wang, Y., Neville, A., Hua, Y., 2021. Revealing the temperature effects on the corrosion behaviour of 2205 duplex stainless steel from passivation to activation in a CO2-containing geothermal environment. Corros. Sci. 187, 109495.
Matsuo, D., Arai, Y., Kanki, K., Sagara, M., Amaya, H., 2022. Corrosion resistance of super duplex stainless steel for CCS usage under supercritical CO2 conditions with impurity gas. In: Proceedings of the AMPP Annual Conference+ Expo. San Antonio, TX. OnePetro, 17602.
Nilsson, J.O., 1992. Super duplex stainless steels. Mater. Sci. Technol. 8, 685–700.
Nordsveen, M., Nešić, S., Nyborg, R., Stangeland, A., 2003. A mechanistic model for carbon dioxide corrosion of mild steel in the presence of protective iron carbonate films–part 1: theory and verification. Corrosion 59, 443–456.
Sathirachinda, N., Pettersson, R., Wessman, S., Kivisäkk, U., Pan, J., 2011. Scanning Kelvin probe force microscopy study of chromium nitrides in 2507 super duplex stainless steel–implications and limitations. Electrochim. Acta 56, 1792–1798.
Soares Costa, J., Altenhofen, A., 2024. Corrosion behavior of supermartensitic stainless steel 13Cr and stainless steel 316L under chloride solution and H2S/CO2 environments. Corrosion 80, 880–888.
Sun, H., Wang, H., Zeng, Y., Liu, J., 2023. Corrosion challenges in supercritical CO2 transportation, storage, and utilization–a review. Renew. Sustain. Energy Rev. 179, 113292.
Svenningsen, G., Morland, B.H., Bonfanti, R.O., 2023. Corrosion testing of CRA in simulated CO2 injection well environments. In: Proceedings of the AMPP Annual Conference + Expo. Denver, CO. AMPP, 18993.
Turnbull, A., Griffiths, A., 2003. Review: corrosion and cracking of weldable 13 wt-%Cr martensitic stainless steels for application in the oil and gas industry. Corros. Eng. Sci. Technol. 38, 21–50.
Wei, L., Gao, K., 2019. Understanding the general and localized corrosion mechanisms of Cr-containing steels in supercritical CO2-saturated aqueous environments. J. Alloys Compd. 792, 328–340.
Wei, L., Pang, X., Gao, K., 2016. Corrosion of low alloy steel and stainless steel in supercritical CO2/H2O/H2S systems. Corros. Sci. 111, 637–648.
Yue, X., Zhang, L., Ma, L., Lu, M., Neville, A., Hua, Y., 2021. Influence of a small velocity variation on the evolution of the corrosion products and corrosion behaviour of

super 13Cr SS in a geothermal CO2 containing environment. Corros. Sci. 178, 108983.
Yue, X., Zhang, L., Wang, Y., Xu, S., Wang, C., Lu, M., Neville, A., Hua, Y., 2020. Evolution and characterization of the film formed on super 13Cr stainless steel in CO2-saturated formation water at high temperature. Corros. Sci. 163, 108277.
Zhang, Z., Ding, C., Liu, W., Zhao, Y., 2024. Study on corrosion of Cr-containing steel under different CO2 partial pressures at high temperatures. Geoenergy Sci. Eng. 243, 213365.
Zhao, Y., Xie, J., Zeng, G., Zhang, T., Xu, D., Wang, F., 2019. Pourbaix diagram for HP-13Cr stainless steel in the aggressive oilfield environment characterized by high temperature, high CO2 partial pressure and high salinity. Electrochim. Acta 293, 116–127.
Zhu, J., Li, D., Zhang, Y., Zhang, L., 2019. Effect of extremely high CO2 pressure on the formation of the corrosion film on 13Cr stainless steel. RSC Adv. 9, 38597–38603.